Molecular and Nano-engineering with iron, ruthenium and carbon: Hybrid structures for sensing

Geest, E.P. van

Chapter 1

Introduction

Molecular and Nano-Engineering with Iron, Ruthenium and Carbon: Hybrid structures for Sensing

1.1. Graphene and metal complexes: tools for engineers

Through careful monitoring of vital signs and biomarkers, healthcare has been able to skyrocket to the high level it is today. Personalized healthcare could alleviate drug side effects and strict conditions (*i.e.* long hospitalization, or heavy periodical treatments like dialysis) of a patient through an optimized treatment scheme. This requires highly sensitive and accurate sensors. In 2004, graphene has emerged, a single sheet of graphite with a honeycomb arrangement of sp^2 carbon atoms, which could very well be a key player in the development of next-generation sensors. Graphene, a semiconducting 2D material with properties that are very suitable for electrical engineering, for example for sensing technologies, has the potential to fulfill the demands of modern sensors for selectivity and sensitivity.

Yet, a single graphene sheet is in fact not very useful in electronic sensors. The sensitivity and selectivity of graphene-based sensors almost completely depends on what is present on this 2D sheet: the coating, or functionalization, of graphene should be chosen specifically to provide a graphene-based sensor with sensitivity and selectivity. This PhD thesis especially focuses on functionalizing graphene-based devices with metal complexes. The chemical versatility of metal complexes is wide, as for instance the nature of the metal, its oxidation state, and the ligands bound to it, altogether determine the properties of each metal complex. These metal complexes can be tuned by molecular design to get specific functions that are useful for the fabrication of selective devices. Among the many properties that have been ascribed to metal complexes, some are technologically more interesting, for example molecular switching of the spin of the complex, or photosubstitution of specific ligands. Both are examined in more detail throughout the chapters of this thesis, with a particular focus on using such properties for sensing with graphene-based devices.

1.2. Engineering with carbon – graphene based sensors

1.2.1. A brief introduction of graphene

Since its recognition, graphene has claimed its fair share of research interest. Graphene is a monolayer of sp^2 carbon atoms of infinite size. While graphite as a bulk material is an everyday commodity since ancient times, the extraction and characterization of a single crystalline honeycomb-structured carbon monolayer has only been achieved in 2004 by exfoliation of highly oriented pyrolytic graphite (HOPG). The first pieces of graphene were prepared by mechanical exfoliation and were micrometer-sized.[1] Various synthetic methods for graphene have since then been developed, and sheets up to 30 inch wide have already been prepared.[2] Its synthesis at such a large scale has opened new routes to use this 2D material in numerous macroscopic devices. Pristine graphene exhibits unique electronic properties, but in most graphene-based devices, graphene requires to be functionalized chemically or physically with molecules or (nano)particles to function.[3] It should be noted here that, although pristine graphene is commonly pictured as a perfect honeycomb structure made of carbon atoms, usually defects in this lattice exist, *e.g.* grain boundaries (where two graphene crystals meet) and (pin)holes, which affect the electronic properties of graphene (see Figure 1.1).[4]

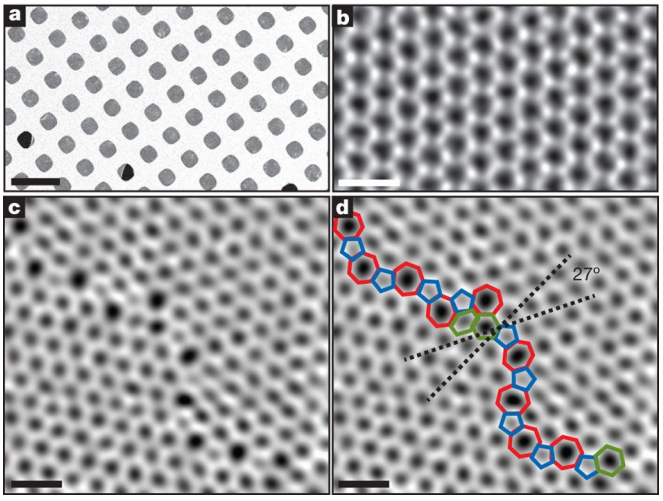

Figure 1.1: Annular dark-field scanning transmission electron microscopy (ADF-STEM) images of a monolayer graphene crystal. A) Graphene on a TEM grid, scale bar = 5 μm. B) The hexagonal structure of pristine graphene. C and D) Grain boundary in graphene, where the honeycomb structure is disrupted (coloured rings). B-D: scale bar = 5Å. Reprinted with permission from Huang et al., © Nature, 2011.[4]

Graphene can be synthetized using various techniques, and the technique that is used will drastically influence the performance of the resulting graphene-based sensor. Synthetic approaches that yield pristine graphene are mechanical exfoliation[1], chemical vapor deposition growth[5] (CVD graphene) on a metal surface, and bottom-up synthesis[6] from aromatic precursors. A common approach to produce graphene in bulk is the oxidation of graphite into graphene oxide (GO, an electrical insulator) using Hummer's method, an aggressive oxidation approach.[7] The oxidized graphene flakes are then reduced chemically or thermally, yielding reduced graphene oxide (rGO). A clear distinction should always be made between pure graphene and rGO, as reduction of GO will never be complete; a certain amount of oxidation moieties will always remain at the surface and edges.[8] rGO typically shows far lower conductivity than exfoliated or CVD-grown graphene and could thus be considered less suitable for use in electronic sensors than pristine graphene.[9]

1.2.2. Electronic properties of pristine graphene

The properties of graphene originate mainly from the molecular arrangement of its sp^2 carbon atoms. The 2D honeycomb structure (which can be described as two overlapping triangular lattices with 2 atoms per unit cell; see Figure 1.2A) is hexagonal. The Brillouin zone of the graphene lattice is also hexagonal, however its corners **K** and **K'** are not equivalent. **K** and **K'** are called Dirac points; at these points the Dirac cones for electrons and electron holes contact each other (see Figure 1.2B).[10] At the Dirac cones the valence and conducting electronic bands of graphene meet. Since these bands connect, but do not overlap, graphene is considered a zero-gap semiconductor.

In theory, 'perfect' graphene in an electrically and magnetically neutral environment does not exhibit electric conductivity at 0 K. At these conditions, the Fermi level lies exactly between the two electronic bands. Here the valence band is completely filled, while the conductance band is completely empty. [10, 11] Without a partially filled electronic band there are no charge carriers, *i.e.* free electrons in the conductance band or electron holes in the valence band, and electrical resistance of the graphene sheet is maximal. The Dirac point is indeed represented by a resistance maximum in a resistivity (ρ) *vs.* gate voltage (V_g) plot (see Figure 1.2C).[12] The gate voltage creates an electric field, to which the graphene sheet is sensitive, and as V_g moves away from the Dirac point, charge

carriers are created and graphene becomes conductive. Graphene therefore is a special kind of electrical material, showing both p- and n-type semiconductor character, depending on the sign and value of V_g.

The gate voltage dependence of the electric properties of graphene is exploited in graphene field-effect transistors (GFETs) produced from the single atom-thick carbon sheet. A typical GFET is shown schematically in Figure 1.2D. A graphene sheet is positioned on a silicon wafer of which the surface is a layer of the electrically insulating SiO_2 of ~300 nm thickness. The gate potential is applied to the silicon back side, creating an electric field through the SiO_2 layer. The graphene sheet is electrically connected through the source and drain electrodes, typically via nanometer-thick gold strips. The transistor is in ′off′ mode at the Dirac point, where graphene is an insulator, and in "on" mode when V_g is far away from the Dirac point and graphene is conductive.[13]

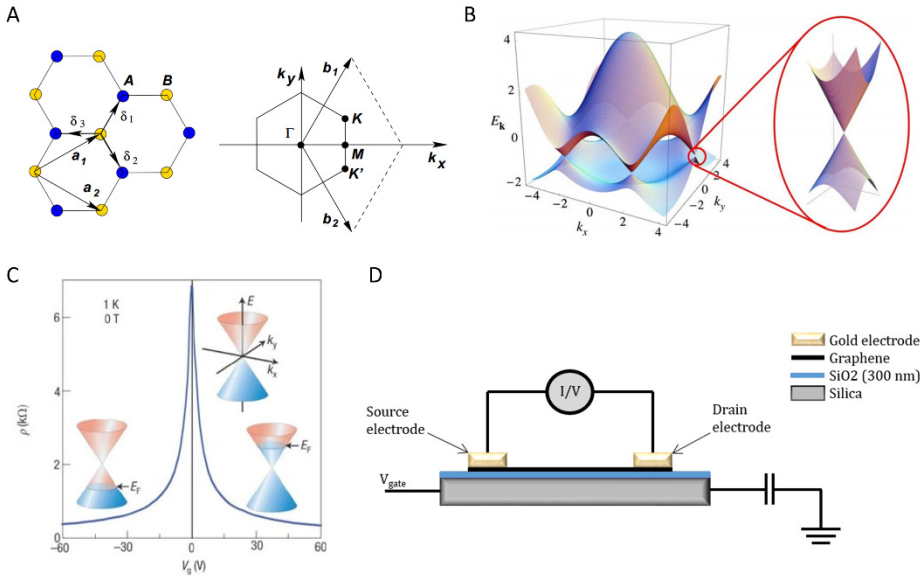

Figure 1.2: Electronic properties of graphene. A) Honeycomb lattice and Brillouin zone for graphene. B) Electronic dispersion in the Brillouin zone from pristine graphene. The conducting and the valence electronic bands meet at the Dirac point (zoom). Figure 1.2A and B reprinted with permission from Castro Neto et al., © American Physical Society, 2009.[11] C) Resistivity (ρ) as a function of gate voltage (V_g) for pristine graphene at 1 K. Dirac cones are showed at a negative, positive and zero value of the applied gate voltage. Reprinted with permission from Geim et al., © Nature, 2007.[12] D) Schematic view of a graphene field-effect transistor (GFET). A silicon wafer is used as the (back) gate in typical GFETs.

1.2.3. Sensitivity of graphene and sensor technology

Graphene-based devices are known to be sensitive to changes in the environment of the 2D carbon sheet, more specifically to dipole changes near the graphene surface.[9] This opens a way for graphene devices to be used as sensors. For example, a GFET made of pristine graphene was able to detect the absorption of NO_2, even at the single molecule level. The sensitivity of this GFET sensor was attributed to the high surface-to-volume ratio, high conductivity, low defect concentration of the graphene 2D crystal, and the ability to do four-terminal sensing (using four electrodes instead of two for electrical measurements to eliminate contact resistance, which gives more precise measurements with it).[14]

Being atomically thin, graphene and other 2D materials exhibit surface-to-volume ratios higher than any 3D material. In fact, the entire volume of the carbon material is exposed to an adsorbent to be detected, maximizing the sensing effect. Due to its high, metallic-like electrical conductivity (*i.e.* the Fermi level is in at least one energy band) and low noise levels (Johnson noise, *i.e.* electric noise generated by thermal agitation of the charge carriers, and 1/f noise, particularly for few-defect single crystals) graphene raised special interest for its implementation in sensing technologies.[15] Low electric noise levels increase the signal-to-noise ratio, and thus increase the sensitivity of the sensing device.

In fact, the 2D nature of graphene can also be used for sensing. Nanopores in graphene membranes for example have been proposed for DNA sequencing by measuring the ionic current through the pore, *i.e.* the current generated by charged ions moving from the *cis* to the *trans* chamber of a flow cell driven by an electrostatic potential (see Figure 1.3A).[16] When DNA is located in the nanopore, this ionic current is blocked, which can be observed as a current drop in the ionic current measurements. In theory each nucleotide blocks this current differently, and thus individual nucleotides may be identified. Currently, DNA sequencing is done in the clinics with biological nanopores (Oxford Minion) using this principle.[17]

Solid-state nanopores, like graphene nanopores, have the advantage over biological pores (which are used in the Minion devices) that they can be precisely shaped and fabricated on a large scale and have a high chemical, thermal and mechanical stability.[18] A rule of thumb for nanopore-based DNA sequencing dictates that the smaller the membrane, the higher the resolution of sensing is (as

the total current blockade originates from less nucleotides that are in the pore at the same time, see Figure 1.3B). Graphene-based nanopore devices, using an atomically thin membrane, can theoretically be used to obtain the highest possible base-calling accuracy (*i.e.* individual nucleobase readout) in DNA sequencing.[16] The major drawback of solid-state nanopores is, however, the high speed of the DNA strand as it passes through the pore; current equipment for electrical measurements cannot measure within the time frame that is required to identify a single base passing through the pore.[19] In Chapter 6, we describe how we aimed to use a ruthenium complex to control the speed of DNA through a nanopore using thermal binding of the ruthenium complex to DNA and its photoactivated release.

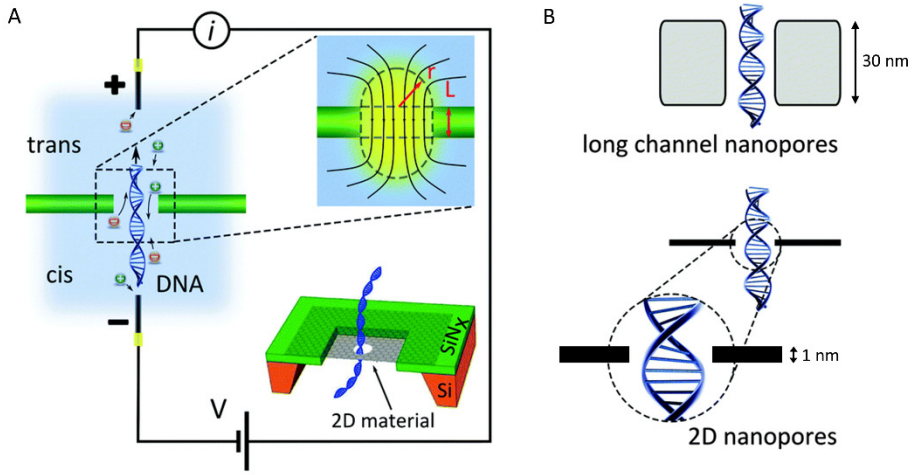

Figure 1.3: Nanopores for DNA sequencing. A) Operating principle of a nanopore device for DNA sequencing. As DNA travels through a nanopore, an ionic current from the *cis* to the *trans* chamber (or *trans* to *cis* for oppositely charged ions) of a flow cell is blocked, which is measured electrically. B) The thickness-resolution rule of thumb: the smaller the membrane with the pore, the less bases are measured at the same time: in thick pores (top, squares represent ~30 nm membrane), many DNA bases block the pore, while for thin membranes (bottom, lines represent ~1 nm membrane), only a small number of bases block the pore. Figure adapted from Arjmandi-Tash et al., © Royal Society of Chemistry, 2016.[16]

1.2.4. Graphene functionalization

Graphene-based sensors usually function via the sensitivity of the graphene sheet to functional molecules or particles attached to or deposited on the surface of graphene.[9] Placing a functional molecule on the surface of graphene is often referred to as graphene functionalization, and can be categorized into two main

classes, covalent and non-covalent functionalization (sometimes intercalation, which is also non-covalent, is mentioned as a third class), which refers to the binding interactions between the functionalizing molecules or nanoparticles and the graphene surface (see Figure 1.4). One of the consequences of covalent binding in particular, is that the the structure of the graphene lattice is permanently affected, hence its electrical properties. Non-covalent functionalization on the other hand changes the conductivity of graphene but does not change the lattice of graphene (as the conjugation of the 2D network of sp^2 carbon atoms remains intact).[3]

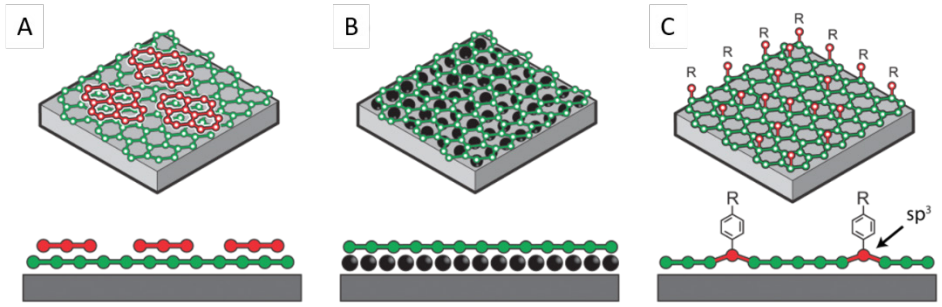

Figure 1.4: Graphene functionalization approaches, classified based on the mode of binding. A) Non-covalent functionalization. B) Intercalation. C) Covalent functionalization. Adapted from http://surfchem.dk/research/projects/graphene-chemistry/, accessed 17-03-2020.

The conjugated C-C double bonds of the graphene basal plane could be used for the covalent attachment of functional moieties through chemical reactions, for example through nucleophilic addition,[20] 1,3-cycloaddition,[21] and free radical reactions with diazonium salts.[22] Another common strategy for covalent functionalization is to use plasma chemistry, for instance to use O_2 plasma to introduce oxygen containing groups, *i.e.* hydroxyl and epoxide moieties at the surface and carboxylic acid groups at the edges of the sheet.[23, 24] Similarly, fluorine and nitrogen-containing groups were introduced on the surface of graphene by its treatment with their corresponding plasmas.[24] In a different approach, hydrogenation of graphene was done electrochemically, effectively introducing sp^3 hybridized centers in the carbon plane.[25] The graphene surface can also be electrochemically functionalized with aryl groups by applying a potential on graphene, used here as an electrode in an aqueous solution of an aryl iodonium or diazonium salt.[26]

When the intrinsic semi-conductive properties of graphene should absolutely be maintained, while functionalization of its surface is desired, non-covalent functionalization is usually the preferred strategy. This type of surface modification does not induce chemical alteration of the 2D network of sp^2 carbon centers; instead, it exploits supramolecular interactions, *e.g.* van der Waals forces and π-π interactions, to attach functional moieties on the carbon surface. Typically, large aromatic anchors are used, like polyaromatic hydrocarbons (PAHs), to fix molecules to a graphene surface. A common PAH used in this approach is pyrene, which sticks to the graphene plane by π-π stacking. The binding energy of this interaction was calculated to be -1.09 eV (about one-third of the binding energy of the C-C bond in ethane, which is -3.91 eV[27]), at a graphene-pyrene distance of 3.45 Å.[28] Many studies have used the pyrene-based anchoring method to produce functional graphene devices; only a few of them will be mentioned here. For example, the surface of graphene could be functionalized with sensing molecules, for the sensing of *e.g.* glucose[29] and μRNA (see Figure 1.5).[30]

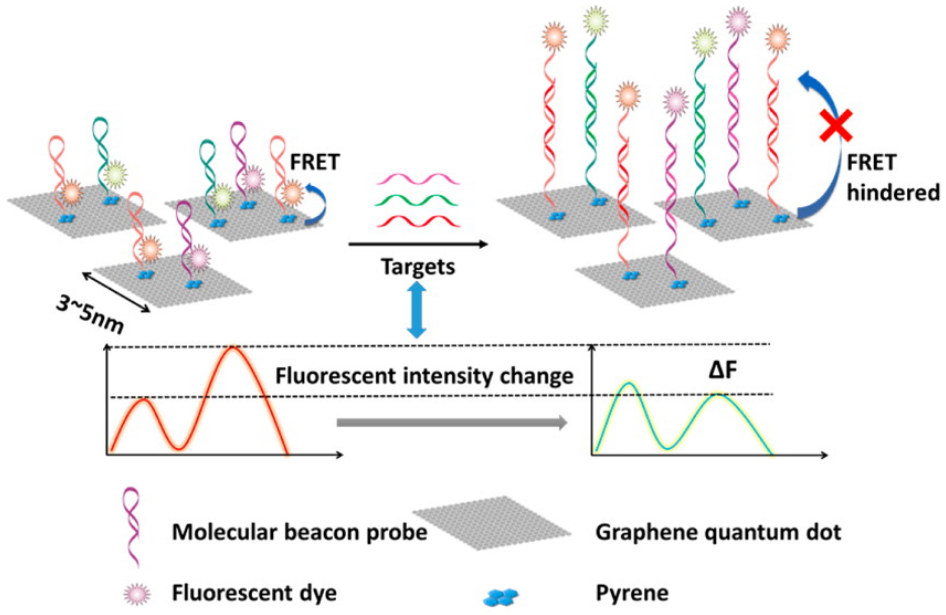

Figure 1.5: μRNA sensing with a graphene device. Molecular probes, short RNA strands terminated with a fluorescent dye at one end and pyrene at the other end, are fixed to on graphene quantum dots. Introduction of target μRNA activates the fluorescence of the dye. Reprinted with permission from Zhang et al., © American Chemical Society, 2015.[30]

Introduction of light-sensitive complexes and particles with pyrene anchors gave rise to devices with widely varying functions. Photoswitching events were observed on graphene when it was functionalized with a zinc spirophan-pyrene complex,[31] from which Zn^{2+} dissociated upon irradiation and coordinated in the dark, and with ruthenium bis(bipyridyl)-pyrene complexes, which induced a photocurrent across graphene when the device was irradiated with light.[32] In others studies, the fluorescence of free silicon nanocrystals and PbS nanoparticles, both functionalized with pyrene moieties, was quenched when they were placed on graphene, effectively providing the carbon sheet with light-harvesting properties.[33]

The examples mentioned here are the tip of the iceberg: functionalization of graphene plays a major role in the function of the device that is fabricated. There are many options to functionalize graphene and to design operational devices, some of which were exploited for the graphene-based sensors described in this thesis. In Chapter 2, in particular, it is described how graphene-based devices can react to molecular switches, even from a distance. We found that graphene field effect transistors reacted strongly to phase transitions in a crystal on which they were fabricated. This crystal was a single crystal of an iron compound that undergoes spin crossover.

1.3. Iron complexes as molecular switches: spin crossover

1.3.1. Magnetic switching in transition metals

In 1931, Cambi and Szegö were the first to write about dithiocarbamate iron(III) complexes showing anomalous magnetic properties.[34] Later, the term 'spin crossover' (SCO for short) was coined for this magnetic switching behaviour, and reports on new SCO complexes based on *e.g.* Ni(II),[35] Co(II),[36] Fe(II),[37] Fe(III),[38] and Mn(II)[39] appeared at a high pace.

A complex that exhibits SCO is able to drastically alter its magnetic, optical, dielectric and mechanical properties, without altering its chemical composition.[40] SCO typically occurs upon external perturbation, *e.g.* a temperature change,[41] irradiation with light,[42] pressure variations,[43] the application of a magnetic field,[44] or an electrical potential.[45, 46] The SCO phenomenon originates from the electronic sphere of a metal center, typically a first row transition metal center with d^4 - d^7 electronic configuration and octahedral coordination sphere. Such

metal centers have 5 d-orbitals, which are divided into two subgroups, the nonbonding t_{2g} orbitals (d_{xy}, d_{yz} and d_{xz}) and the antibonding e_g orbitals (d_{z2} and d_{x2-y2}). Naturally, the non-bonding orbitals are lower in energy than the anti-bonding orbitals; hence an energy gap exists between the subgroups. The size of this energy gap, the ligand field splitting Δ, is determined by the ligand coordination sphere.[47] To explain spin crossover, electron pairing should also be considered. The pairing of two electrons in a single molecular orbital requires that the spins of both electrons are opposite to each other, according to Pauli's principle. However, having two opposite spins brings an energetic cost; thus electrons tend to spread across degenerate orbitals (orbitals with the same energy) as much as possible to minimize spin pairing.[48]

Distribution of the d-electrons over the t_{2g} and e_g orbitals is governed by minimizing the Gibbs free energy ΔG, which has an enthalpy (ΔH) and an entropy (ΔS) contribution, where $\Delta G = \Delta H - T\Delta S$ (see Figure 1.6). At a low temperature (T), the entropy contribution is low, since it is linearly correlated to the temperature, and the enthalpy is the dominating part of ΔG. The low spin (LS) state, *i.e.* $^1A_1$ for Fe^{II}, with six d electrons paired up in the t_{2g} orbitals, is favored under these conditions. This is the diamagnetic phase of Fe^{II}-based SCO material (total spin $S = 0$). The paramagnetic high spin (HS) state ($^5T_2$ for Fe^{II}, with a total spin $S = 2$ and the electrons distributed in an unpaired fashion) on the other hand, is favored at high temperatures, as this state is more disordered than the low spin state (as metal to ligand bonds have lengthened). At the SCO transition temperature, the entropy contribution to ΔG equals the energy barrier from the LS to HS conversion (which originates mainly from the energy required to place the electrons in the higher e_g orbitals). When reaching this temperature in the heating mode, the sign of ΔG for this conversion changes from positive to negative, making the transition from LS to HS thermodynamically favoured, upon which the system switches to the high spin state.[49, 50]

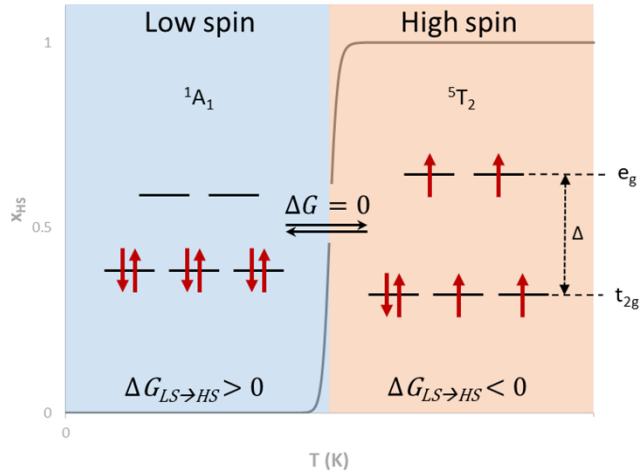

Figure 1.6: Schematic overview of spin crossover according to the ligand field theory. At low T, the low spin state $^1A_1$ is favored due to a large negative enthalpy ΔH contribution to ΔG. When T increases, the higher entropy of the high spin state $^5T_2$ brings ΔG to negative values and hence drives the spin state equilibrium towards the right.

1.3.2. Types of spin crossover behaviour and cooperativity

The spin crossover behaviour is not the same for each species that exhibits this phenomenon. The various behaviours of thermal SCO can be categorized into five classes, illustrated by the temperature evolution of the product of their molar magnetic susceptibility (χ_m) multiplied by the temperature (*i.e.* $\chi_m T$), or in a more simplified way, by the temperature evolution of the fraction of high spin molecules (γ_{HS}) in the sample (see Figure 1.7). We distinguish between gradual, abrupt, hysteretic, multi-step, and incomplete spin crossover. While during gradual spin crossover the phase transition occurs smoothly over a wide temperature range (>100 K), during abrupt transitions the transition is sharp and takes place over a short temperature range (<10 K).

Hysteresis is defined by cases where SCO occurs at a lower temperature when cooling the material than when heating the material. In such a case a hysteresis cycle opens over a temperature range that can span from a few degrees to 50 K or more. A hysteresis cycle is an indication of the existence of two metastable phases, one HS and one LS, which can co-exist at one given temperature. HS and LS complexes may also co-exist in a mixed intermediate spin phase, which appears for compounds showing multiple-step SCO. Finally, incomplete SCO are observed when the SCO compound does not reach full LS phase at low

temperatures, *i.e.* when γ_{HS} in the material never reaches 0 upon cooling.[50] Combinations of the different SCO types described above can exist as well. For example, single crystals of [Fe(bapbpy)(NCS)$_2$] (where bapbpy = N,N'-di(pyrid-2-yl)-2,2'-bipyridine-6,6'-diamine) display curious SCO behaviour. Single crystals of this complex exhibit SCO in a two-step-with-hysteresis fashion, with next to the HS and LS phase (phase I and III, respectively) an intermediate spin phase (phase II) where the ratio of molecules in the HS and LS state is 1:2. The transitions of the single crystal, phase I to II and phase II to III, are both abrupt and with hysteresis.[51]

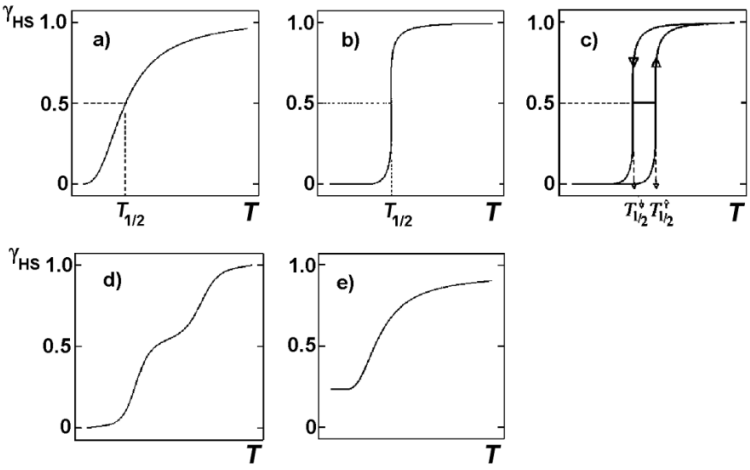

Figure 1.7: Different classes of spin crossover behaviour. Mole fraction γ_{HS} *vs.* T profiles of the different classes of spin crossover behaviour: gradual (a), abrupt (b), with hysteresis (c), multi-step (d) and incomplete (e). Reprinted with permission from Gütlich et al., © Beilstein-Institut, 2013.[50]

The behaviour of SCO in a material is highly controlled by "cooperativity". Cooperativity in this sense refers to the degree of interaction of an individual SCO molecule with its neighbors in the crystal lattice.[52] In a crystal, a SCO phase transition, which is a 1st order transition, usually nucleates at an edge or a defect in the crystal, then grows through the crystal.[53] Propagation of such a phase transition between two crystallographic phases (where the spin states of the molecules are not identical) defines a spin crossover front that can be seen as the transient region of the crystal where molecules go from one phase to the other. This front propagates in one or the other direction depending on temperature gradient in the sample for example, and propagation of the front is fast or slow depending on whether the interaction, or "communication", between neighboring molecules, is strong or weak.[54]

This cooperativity first of all can come from Van der Waals interactions; since the HS molecule is larger than the LS molecule, switching from LS to HS exerts a pressure on the neighboring molecules (as the HS molecule does not fit anymore in the LS crystal lattice), causing the neighboring molecules to switch as well, resulting in the propagation of the phase transformation through the crystal.[54] Other forms of supramolecular interactions contributing to cooperativity can be hydrogen bonding and π-π stacking interactions. Such interactions were found to be responsible for the cooperativity in for example [Fe(bbpya)(NCS)$_2$] (where bbpya = N,N-bis(2,2'-bipyrid-6-yl)amine), which shows an abrupt spin crossover with hysteresis (see Figure 1.8).[55] Introducing a hydrogen bonding network, incorporation of π-stacking moieties and steric groups, and coordination of bridging ligands in the crystal lattice are common strategies to increase cooperativity in bulk materials.[50, 54, 56] Controlling SCO behaviour in nanomaterials however, requires radically different approaches.

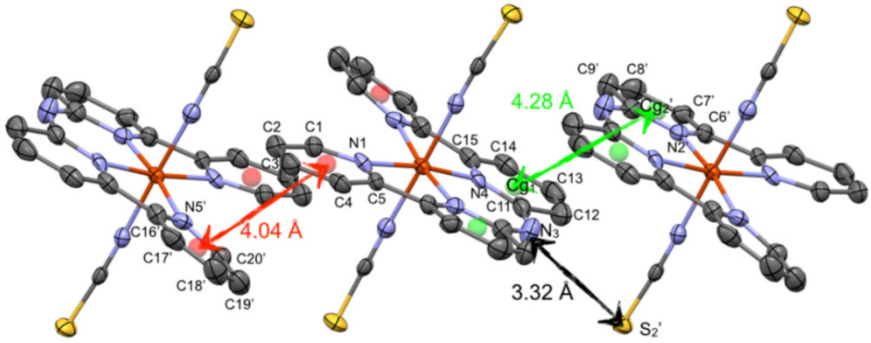

Figure 1.8: X-ray crystal structure of the SCO material [Fe(bbpya)(NCS)$_2$]. The interactions responsible for the cooperativity of this material are hydrogen bonding between H and S (black arrow) and π-π stacking (red and green arrows). Reprinted with permission from Zheng et al., © Wiley, 2015.[57]

1.3.3. Small scale spin crossover: reduced size effect

For spin crossover materials to be used in nanotechnology, the size of the material should be reduced. However, scaling down to the nanometer scale can have a big impact on spin crossover properties. Common observations when scaling down SCO materials to the nanometer scale are hysteresis fading, decreasing spin transition temperatures, and complete transitions becoming incomplete.[58] Theoretical models have been published that allow for explaining these observations.[59] In a nutshell, spin crossover nanoparticles (SCO NPs) are typically a few nanometers in size, and their surface-to-volume ratio, which is

related to the fraction of molecules in the nanoparticle that "feel" the bulk environment, is limited.[60] The SCO properties of the molecules that "feel" the modified surface environment, modify the SCO properties of the nanoparticles as a whole. The size of the nanoparticle has been appointed as critical for maintaining the bulk SCO behaviour in a nanoparticle of the same material, *e.g.* for the 3D metal organic framework [Fe(pyrazine)Pt(CN)$_4$] (see Figure 1.9)[61] and the 1D chain coordination compound [Fe(NH$_2$trz)$_3$]Br$_2$·3H$_2$O (where NH$_2$trz = 4-amino-1,2,4-triazole).[62] For the latter material critical nanoparticle sizes of about 45-50 nm[63] and 30 nm[64] have been reported. While the transition temperature did not change as the size decreased, the transition became less abrupt and the hysteresis loop became smaller when particles decreased in size, and even disappeared for particles of 30 nm.[64] Interestingly, other triazole SCO complexes, *e.g.* [Fe(Htrz)$_2$(trz)](BF$_4$)] (where Htrz = 1H-1,2,4-triazole) showed bulk SCO behaviour (with hysteresis) at much smaller sizes, with an average size of 11 and even 6 nm.[65]

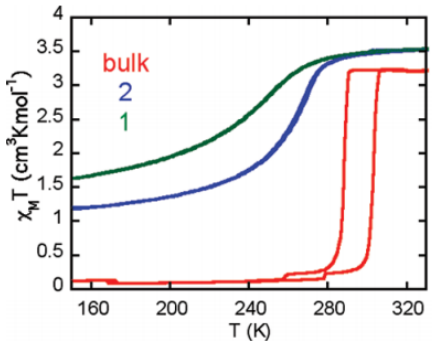

Figure 1.9: Reduced size effect of spin crossover. Magnetic susceptibility versus temperature plot showing the spin crossover behaviour of [Fe(pyrazine)Pt(CN)$_4$] bulk and nanoparticles (1: 7 nm; 2: 14 nm). Reprinted with permission from Volatron et al., © American Chemical Society, 2008.[61]

Interestingly, coating NPs with an (inert) shell may help to retain the bulk SCO properties in the nanomaterial. This wrapping of a SCO NP can influence the SCO behaviour; this phenomenon is called the matrix effect.[66] Strong variations in the spin transition characteristics of [Fe(pyrazine)Pt(CN)$_4$] NPs have been observed when they were coated with various shells. For example, a more elastic matrix leads to more gradual transitions, while a more rigid shell, like SiO$_2$, improved cooperativity and promoted abruptness of the transition and hysteresis.[67] The matrix effect is a strong example of how the environment of an SCO NP can influence its cooperative behaviour.

Instead of nanoparticles, spin crossover compounds can also be grown into thin films with high control over film thickness, which is typically in the nanometer range. For example, a thin film of $[Fe(pz)Pt(CN)_4]$ with nanometer thickness was synthetized directly on a gold surface via layer-by-layer assembly, by sequential dipping of a pre-treated gold substrate into Fe^{2+}, $[Pt(CN)_4]^{2-}$ and pyrazine solutions.[68] Films could also be obtained, down to 7 nm, by evaporation under high vacuum, such as for the SCO complex $[Fe(phen)_2(NCS)_2]$ (where phen = 1,10-phenanthroline),[69] which were still SCO-active. In the end, there is a range of techniques that can be used to produce thin films, *e.g.* spin coating, drop casting, layer-by-layer assembly, vacuum evaporation and Langmuir Blodgett.[70] For thin films however, a similar limitation exists with regards to scaling down to the nano-level: the receiving surface plays a crucial role.

1.3.4. Spin crossover on surfaces

Similar to the matrix effect observed for SCO NPs, a surface in the near proximity of SCO thin layers can also influence the SCO behaviour of the layer. Interactions between the surface and nearby SCO molecules can interfere with or even inhibit spin crossover in these molecules. For example, a thin film of $[Fe(bpz)_2(phen)]$, (where bpz = dihydrobis(pyrazolyl)borate and phen = 1,10-phenanthroline) was produced on a gold surface. Spin crossover occurred in individual molecules of this compound, but once deposited on the gold surface the molecules closest to the surface were unable to flip their spin. In contrast, the 2nd row of molecules did switch their spins, as observed by a change in the dielectric constant associated with SCO. Moreover, they could even be actively switched by applying a potential pulse from the STM tip (see Figure 1.10).[71]

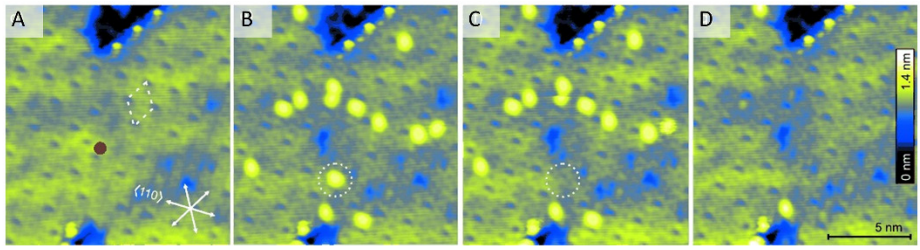

Figure 1.10: Spin switching in molecular thin films. STM image of a $[Fe(bpz)_2(phen)]$ thin film. The monolayer (faint yellow background) does not exhibit spin crossover. When a voltage pulse was applied at the red dot (A), several 2nd row molecules changed their dielectric state (bright yellow dots, B). The circled molecule was switched back to LS by applying a weaker pulse (C); other HS molecules could be returned to LS in the same way (D). Figure adapted from Gopakumar et al., © Wiley, 2011.[71]

When spin crossover nanomaterials are to be implemented in electronic systems, patterning and organization of the particles at the nanoscale is of high importance. Currently, the industry standard for patterning is the lift-off process, which uses a sacrificial photoresist mask to expose the surface only where the mask was developed, *i.e.* by e-beam lithography.[72] Patterning of [Fe(pyrazine)Pt(CN)$_4$] particles was achieved with sub-10 nm precision using this technique.[73] Micro-contact printing on the other hand uses a polymeric stamp to produce a pattern on a surface. In this way, a patterned monolayer of SCO NPs was deposited on nano-spaced gold electrodes, yielding devices that showed hysteresis near room temperature in I/V curves, corresponding to the SCO behaviour of the nanoparticles.[46, 74] These are just two examples of a range of patterning techniques that can be applied to implement SCO nanomaterials in functional devices. In Chapter 3 of this thesis it is described how we used patterning for selective growth of thin films based on the SCO complex [Fe(bapbpy)(NCS)$_2$.

1.3.5. The other challenge of SCO nanomaterials

Although producing thin films and nanomaterials with SCO properties and implementing them in electronic devices are challenges by themselves, analysis of spin crossover materials at the nanoscale can be equally a challenge and may require some unconventional techniques. Magnetic susceptibility measurements with a SQUID, typically used to analyze bulk SCO samples, is very challenging for thin films or for measuring the SCO of several NPs, as the amount of material is very small. To monitor SCO in thin films, surface analysis techniques may be more suitable, *i.e.* Surface Plasmon Polariton Resonance (SPPR),[75] (Surface Enhanced) Raman Spectroscopy (SERS),[68, 76, 77] and Surface Plasmon Resonance (SPR).[76] Other techniques to observe SCO in nanoparticles (on surfaces) are Scanning Tunneling Microscopy (STM)[71] and Current Imaging Tunneling Spectroscopy (CITS).[78] Moreover, SCO could be observed through electrical measurements by connecting single particles[46] and single molecules[79] between nanometer-spaced electrodes; however this is technically difficult. These examples show that, although challenging, analysis of SCO nanomaterials can be done. In the end, integration of SCO (nano)materials in electronic devices remains challenging, and showing in a convincing way that the SCO of the materials in these devices is responsible for their electronic response, perhaps even more. Yet, the field continues to advance in connection with device engineering, highlighting the technological interest in spin crossover materials.[80]

1.4. Ruthenium complexes – a matter of light and dark

1.4.1. Light-powered molecular switches

Going one step down from iron in the periodic table, is an element that also switches: ruthenium. Ruthenium polypyridyl complexes are known to react strongly to visible light by changing their chemical structure, while when irradiation is shut off, they may return to their dark state, thus realizing a light-responsive chemical equilibrium. Particularly representative examples of light-sensitive ruthenium complexes, that show some similarity to the switching behaviour of spin crossover complexes, are ruthenium(II) polypyridyl sulfoxide and sulfone complexes that may do phototriggered S → O linkage isomerization, either in solution or within a crystal lattice.[81] Spin crossover and linkage isomerization materials are indeed two well-studied examples of single-crystal-to-single-crystal transformations[82] and were both used to fabricate mechanical actuators.[83]

In phototriggered linkage isomerization, the coordination mode of for example a dimethylsulfoxide (DMSO) ligand to the ruthenium(II) center changes, upon visible light irradiation, from a sulfur-bound mode to an oxygen-bound mode (see Figure 1.11). While doing so, the bulk properties of a single crystal of this compound (its color, for example) change as a result of molecular changes within the crystal lattice.[81] Complexes capable of linkage isomerization act as molecular switches, as do spin crossover complexes, and they may also be integrated as light-responsive switches in devices.

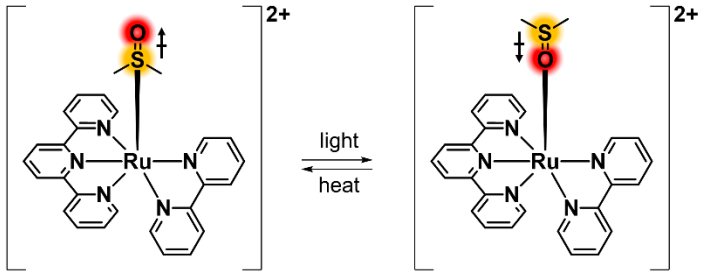

Figure 1.11: Phototriggered linkage isomerization. The DMSO ligand in $[Ru(tpy)(bpy)(DMSO)]^{2+}$, where tpy = 2,2′:6′2″-terpyridine and bpy = 2,2′-bipyridine, changes from S-bound to O-bound upon irradiation (S and O are indicated in yellow and red, respectively).[81] The dipole moment of the DMSO ligand is indicated by the arrow.

1.4.2. Light-driven ligand exchange

Phototriggered linkage isomerization represents, however, only one of the multiple photochemical conversions that may occur when ruthenium polypyridyl complexes are irradiated with visible light. In particular, photosubstitutionally active ruthenium polypyridyl complexes exchange one (or more) ligand of their coordination sphere, by a solvent molecule, upon visible light irradiation.[84] For example, irradiation of ruthenium polypyridyl complexes with monodentate thioether- or pyridine-based ligands leads to the dissociation of these monodentate ligands in solution, while in the dark the photodissociated ligand can coordinate back to the ruthenium center in a thermal substitution reaction.[85] Like linkage isomerization, such systems can be described as a chemical equilibrium that is shifted by light irradiation. Figure 1.12 shows the Jablonski diagram for ruthenium polypyridyl complexes that are capable of photodissociating a ligand. Upon irradiation, the ground state ^{1}GS is excited to a metal-to-ligand charge transfer excited state (^{1}MLCT), followed by intersystem crossing to the corresponding triplet (^{3}MLCT) state. From this state, one or several ligand-field (^{3}LF) excited state can be reached thermally if the energy gap between the ^{3}MLCT and ^{3}LF states is sufficiently small; such internal conversion results in ligand dissociation.[86]

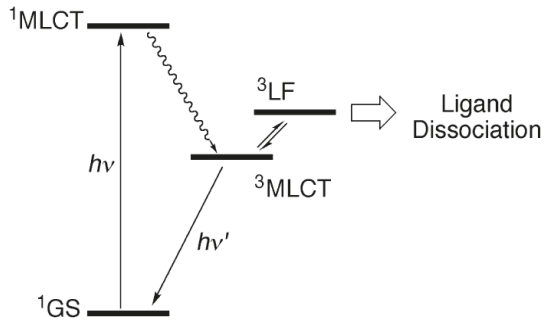

Figure 1.12: Typical Jabsonski diagram for photosubstitutionally active ruthenium polypyridyl complexes. Reprinted with permission from Garner et al., © American Chemical Society, 2011.[86]

1.4.3. Photosubstitution for therapy – ruthenium-based drugs

Photosubstitution processes raised attention in anti-cancer research, and led to prodrugs that can be switched on by *in situ* light irradiation at the tumor site. The switching of the biological activity of a ruthenium-photocaged drug is a treatment

modality often called "photo-activated chemotherapy" (PACT).[87] In PACT, a cytotoxic compound is "caged" by carrier complex, for instance a photosubstitutionally active ruthenium complex. When this compound is caged, it is inactive and not toxic to cells. Through irradiation, the compound can be photosubstituted, which unlocks its ability to kill the cell.[87] PACT provides hence irradiation-based selectivity of the drug towards (malignant) cells, as only irradiated cells are attacked by the activated compound, which leaves healthy, non-irradiated cells, intact.

However, a challenge in PACT is to determine where irradiation should occur, as most PACT compounds are not emissive. To solve this issue, a PACT compound was functionalized with a group that provides fluorescence only after drug cellular uptake, which can help to determine where irradiation should occur (see Chapter 7 of this thesis). In this work the ruthenium complex is a non-toxic "caging" group, and the photosubstituted ligand, a cytotoxic active pharmaceutical ingredient. One should realize though, that although a ruthenium "caging" complex may be relatively harmless as compared to the uncaged species, the complex may still interact with cellular components after it has photoreleased its cargo.

1.4.4. DNA binding of ruthenium: probes and sensors

After ligand photosubstitution, the vacant coordination site of a ruthenium complex "opens up" by weak coordination of a water ligand. The weakness of water coordination to ruthenium(II) also means that the ruthenium complex can be involved again in coordination reactions. In *vivo*, likely binding partners are biomolecules, like proteins, lipids, or DNA. More specifically, the interactions of ruthenium complexes with DNA have been studied extensively for their potential use in therapy and bio-imaging.[88] Coordination reactions entail the direct binding of the metal center to nitrogen atoms of the DNA base pairs, which can be selective for certain nucleobases. For example, ruthenium(II) arene complexes were shown to bind specifically to the nucleobase guanine, through coordinating to the nitrogen N7 atom.[89] Such ruthenium-purine bonds can in fact be light-sensitive as well, *i.e.* the Ru-N7 coordination bond can be broken upon irradiation with visible light.[90] We re-evaluated this chemistry, and we found that the coordination of dGMP to $[Ru(tpy)(biq)(OH_2)]^{2+}$, where tpy = 2,2′:6′2″-terpyridine, biq = 2,2′-biquinoline, is reversible with green light (see Chapter 6).

Next to direct coordination of nitrogen atoms from DNA to the metal center, ruthenium polypyridyl complexes can also bind to DNA via supramolecular interactions, which may involve either electrostatic interactions, hydrophobic interactions with the minor or major groove of the DNA strand, or intercalation of the ruthenium-coordinated aromatic ligands between the DNA base pairs.[88] In some cases, the photophysical properties of ruthenium polypyridyl complexes were shown to change dramatically when they interacted with DNA. These complexes were therefore studied extensively as molecular probes for DNA sensing and nuclear imaging.

A famous example of imaging with a ruthenium DNA probe is based on the "light switch" effect, a massive increase of the phosphorescence of Ru^{II}(dppz)-based complexes (where dppz = dipyrido[3,2-a:2′,3′-c]phenazine, see Figure 1.13A) upon intercalation of dppz into the DNA helix. As the dppz ligand inserts in the double strand, or even specifically in presence of DNA mismatches, the ruthenium complex becomes highly emissive, while in absence of DNA its emission is fully quenched.[91] Through this emission switching, the complex 'senses' DNA, and this phenomenon has been used for example for DNA staining in cells for bio-imaging of the nucleus with confocal microscopy (Figure 1.13B).[92] Similarly, ruthenium complexes could be used to obtain structural information by colorimetric methods. For example, specific groove binding in the minor groove of A/T-rich DNA strands changed the optical properties of ruthenium dimers in solution,[93] while selective binding of the complex $[Ru(bpy)_2(dmdppz\text{-}Br)]^{2+}$ (where dmdppz-Br = 11-Bromo-3,6-dimethyldipyrido[3,2-a :2′,3′-c]phenazine) to G-quadruplex structures resulted in an increase of the emission of this complex.[94]

These examples show that ruthenium complexes can bind to nucleotides and DNA regions selectively, and change their photophysical properties as their molecular environment changes. These properties makes ruthenium polypyridyl complexes especially interesting from a sensing point of view. Hence, we exploited these properties in this work to improve DNA sensing (Chapter 6) and to design a PACT drug that may show where it is located *in vivo*, prior to treatment with light (Chapter 7).

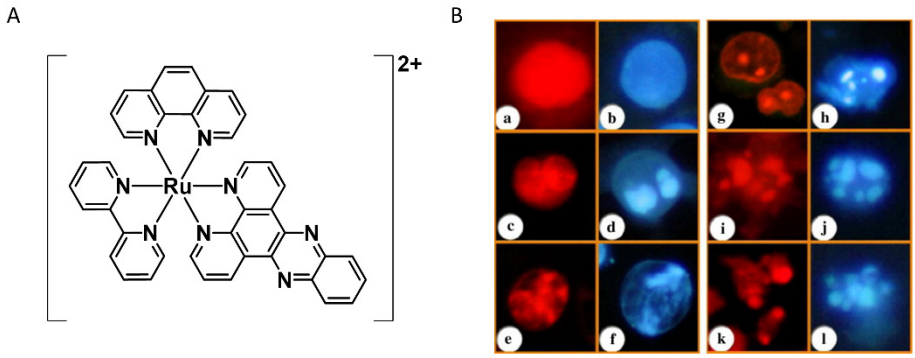

Figure 1.13: "Light switch" effect of DNA intercalation by a ruthenium complex. A) Molecular structure of $[Ru(bpy)(phen)(dppz)]^{2+}$, where bpy = 2,2′-bipyridine, phen = 1,10-phenanthroline, and dppz = dipyrido[3,2-a:2′,3′-c]phenazine. The dppz ligand intercalates in the DNA helix. B). Cell staining of NCI-H460 cancer cells with $[Ru(bpy(phen)(dppz)]^{2+}$ (red panels) and nuclear staining agent Hoechst (blue panels). The cells are going through multiple stages of cell death: healthy cells (a,b), nucleus splitting (c,d) collapsed nucleus (e,f), micronucleus formation (g,h), fragmented multinucleation (i,j) and late apoptotic (k,l). Figure B) reprinted with permission from Rajendiran et al., © Elsevier Inc, 2010.[92]

1.5. Aim of this thesis

The work described in this thesis was aimed at finding out how GFET-based sensors and metal complexes can be used to produce devices for sensing, how metal complexes can improve sensing, and how metal complexes can be used as sensors themselves. First of all, in Chapter 2 we describe how single crystals of the SCO complex $[Fe(bapbpy)(NCS)_2]$ can be integrated in GFET devices that can detect spin switches in a contactless fashion. We found that a new mechanism of sensing, which we called chemo-electric gating, was largely responsible for the variation of the electronic properties of graphene when SCO occurred in the remote crystal. Building on this work, in chapter 3 it is discussed how to obtain nanometer-thick thin films based on the same spin crossover complex using a wet film-growing method.

In chapter 4, we removed the SCO material and discovered it was possible to build graphene sensors that were simply coated with a polymer. Depending on the nature of the polymer such sensors can detect vapours of small molecules by straightforward resistance measurements. Using an array of 3 sensors built with 3 different commercial polymer coatings we could detect and identify a large range of different chemical species.

In chapter 5, we reported GFET sensors that were fabricated on ordinary paper as a substrate. Paper is specifically interesting as a substrate, as its porosity is convenient for sensing in liquids, and it can be bent. We used these GFETs on paper to monitor the interaction between 2-deoxyguanosine monophosphate (dGMP) and a ruthenium complex: the formation of a Ru-N coordination bond in the dark and its cleavage via a photosubstitution reaction in aqueous solutions.

In the work described by the above-mentioned chapters, we used the semiconducting properties of graphene for sensing. In chapter 6, we explored the use of a ruthenium complex in nanopore sensing devices for DNA sequencing. The aim was to use the ruthenium complex to control the speed of DNA translocation through a nanopore using visible light. We envisioned that via thermal binding of a ruthenium complex to DNA in the dark, DNA can be slowed down by the additional friction of the complex. The complex can be released again under irradiation conditions which removes the friction, thus gaining control over the speed of the DNA strand by shining light.

Finally, in chapter 7 we move away from graphene-based sensing devices and into the field of photoswitchable anticancer drugs. A ruthenium complex used to photocage STF-31, a known cytotoxic inhibitor of the metabolic enzyme nicotinamide phosphoribosyltransferase (NAMPT), was equipped with an enzymatically cleavable sensor probe. The fluorescence of the probe is quenched as long as it remained in close proximity to ruthenium. However, ester cleavage by esterase enzymes released the probe from the ruthenium, unlocking its fluorescence. This design is a proof-of-concept for molecules aimed at showing a surgeon where to shine light during phototherapy. *In operando* fluorescence should show where the drug has been taken up by the cancer cells, which may be used to pinpoint where light irradiation should occur to release the cytotoxic drug STF-31, which in turn may cause cancer cell death and tumor regression.

1.6. References

[1] K. S. Novoselov, A. K. Geim, S. V. Morozov, D. Jiang, Y. Zhang, S. V. Dubonos, I. V. Grigorieva, A. A. Firsov, *Science* **2004**, *306*, 666.

[2] S. Bae, H. Kim, Y. Lee, X. Xu, J.-S. Park, Y. Zheng, J. Balakrishnan, T. Lei, H. R. Kim, Y. I. Song, Y.-J. Kim, K. S. Kim, B. Ozyilmaz, J.-H. Ahn, B. H. Hong, S. Iijima, *Nat. Nanotechnol.* **2010**, *5*, 574.

[3] V. Georgakilas, M. Otyepka, A. B. Bourlinos, V. Chandra, N. Kim, K. C. Kemp, P. Hobza, R. Zboril, K. S. Kim, *Chem. Rev.* **2012**, *112*, 6156.

[4] P. Y. Huang, C. S. Ruiz-Vargas, A. M. van der Zande, W. S. Whitney, M. P. Levendorf, J. W. Kevek, S. Garg, J. S. Alden, C. J. Hustedt, Y. Zhu, J. Park, P. L. McEuen, D. A. Muller, *Nature* **2011**, *469*, 389.
[5] Y. Zhang, L. Zhang, C. Zhou, *Acc. Chem. Res.* **2013**, *46*, 2329.
[6] J. Cai, P. Ruffieux, R. Jaafar, M. Bieri, T. Braun, S. Blankenburg, M. Muoth, A. P. Seitsonen, M. Saleh, X. Feng, K. Mullen, R. Fasel, *Nature* **2010**, *466*, 470.
[7] W. S. Hummers, R. E. Offeman, *J. Am. Chem. Soc.* **1958**, *80*, 1339.
[8] K. Erickson, R. Erni, Z. Lee, N. Alem, W. Gannett, A. Zettl, *Adv. Mater.* **2010**, *22*, 4467.
[9] W. Fu, L. Jiang, E. P. van Geest, L. M. C. Lima, G. F. Schneider, *Adv. Mater.* **2017**, *29*, 1603610.
[10] S. Das Sarma, S. Adam, E. H. Hwang, E. Rossi, *Reviews of Modern Physics* **2011**, *83*, 407.
[11] A. H. Castro Neto, F. Guinea, N. M. R. Peres, K. S. Novoselov, A. K. Geim, *Reviews of Modern Physics* **2009**, *81*, 109.
[12] A. K. Geim, K. S. Novoselov, *Nat. Mater.* **2007**, *6*, 183.
[13] F. Schwierz, *Nat Nano* **2010**, *5*, 487.
[14] F. Schedin, A. K. Geim, S. V. Morozov, E. W. Hill, P. Blake, M. I. Katsnelson, K. S. Novoselov, *Nat. Mater.* **2007**, *6*, 652.
[15] K. S. Novoselov, A. K. Geim, S. V. Morozov, D. Jiang, M. I. Katsnelson, I. V. Grigorieva, S. V. Dubonos, A. A. Firsov, *Nature* **2005**, *438*, 197; A. A. Balandin, *Nat. Nanotechnol.* **2013**, *8*, 549.
[16] H. Arjmandi-Tash, L. A. Belyaeva, G. F. Schneider, *Chem. Soc. Rev.* **2016**, *45*, 476.
[17] M. Jain, H. E. Olsen, B. Paten, M. Akeson, *Genome Biol.* **2016**, *17*, 239.
[18] F. Haque, J. Li, H.-C. Wu, X.-J. Liang, P. Guo, *Nano Today* **2013**, *8*, 56; Y. Goto, R. Akahori, I. Yanagi, K.-i. Takeda, *J. Hum. Genet.* **2020**, *65*, 69.
[19] B. Luan, G. Stolovitzky, G. Martyna, *Nanoscale* **2012**, *4*, 1068.
[20] S. P. Economopoulos, G. Rotas, Y. Miyata, H. Shinohara, N. Tagmatarchis, *ACS Nano* **2010**, *4*, 7499.
[21] M. Quintana, A. M. López, S. Rapino, F. M. Toma, M. Iurlo, M. Carraro, A. Sartorel, C. Maccato, X. Ke, C. Bittencourt, T. Da Ros, G. Van Tendeloo, M. Marcaccio, F. Paolucci, M. Prato, M. Bonchio, *ACS Nano* **2013**, *7*, 811; X. Zhang, L. Hou, A. Cnossen, A. C. Coleman, O. Ivashenko, P. Rudolf, B. J. van Wees, W. R. Browne, B. L. Feringa, *Chem. Eur. J.* **2011**, *17*, 8957; V. Georgakilas, A. B. Bourlinos, R. Zboril, T. A. Steriotis, P. Dallas, A. K. Stubos, C. Trapalis, *Chem. Commun.* **2010**, *46*, 1766.
[22] M. Grkovic, D. B. Stojanovic, A. Kojovic, S. Strnad, T. Kreze, R. Aleksic, P. S. Uskokovic, *RSC Adv.* **2015**, *5*, 91280; R. N. Grass, W. J. Stark, M. Fedurco, A. Delfino, J. P. Meraldi, *WO2015193051A1*, **2015**; J. Hong, E. Bekyarova, P. Liang, W. A. de Heer, R. C. Haddon, S. Khizroev, *Sci. Rep.* **2012**, *2*, 624; L. Ren, S. Huang, C. Zhang, R. Wang, W. W. Tjiu, T. Liu, *J. Nanopart. Res.* **2012**, *14*, 1; M. Castelaín, G. Martínez, C. Marco, G. Ellis, H. J. Salavagione, *Macromolecules* **2013**, *46*, 8980; M. B. Lerner, F. Matsunaga, G. H. Han, S. J. Hong, J. Xi, A. Crook, J. M. Perez-Aguilar, Y. W. Park, J. G. Saven, R. Liu, A. T. C. Johnson, *Nano Lett.* **2014**, *14*, 2709.
[23] X. Fang, J. Donahue, A. Shashurin, M. Keidar, *Graphene* **2015**, *4*, 1; S. C. Hernández, V. D. Wheeler, M. S. Osofsky, G. G. Jernigan, V. K. Nagareddy, A. Nath, E. H. Lock, L. O. Nyakiti, R. L. Myers-Ward, K. Sridhara, A. B. Horsfall, C. R. Eddy Jr, D. K. Gaskill, S. G. Walton, *Surf. Coat. Technol.* **2014**, *241*, 8.
[24] B. M. Foley, S. C. Hernández, J. C. Duda, J. T. Robinson, S. G. Walton, P. E. Hopkins, *Nano Lett.* **2015**, *15*, 4876; M. Baraket, S. G. Walton, E. H. Lock, J. T. Robinson, F. K. Perkins, *Appl. Phys. Lett.* **2010**, *96*, 231501.
[25] K. M. Daniels, B. K. Daas, N. Srivastava, C. Williams, R. M. Feenstra, T. S. Sudarshan, M. V. S. Chandrashekhar, *J. Appl. Phys.* **2012**, *111*, 114306.
[26] C. K. Chan, T. E. Beechem, T. Ohta, M. T. Brumbach, D. R. Wheeler, K. J. Stevenson, *J. Phys. Chem. C* **2013**, *117*, 12038; S. Eissa, C. Tlili, L. L'Hocine, M. Zourob, *Biosensors and Bioelectronics* **2012**, *38*, 308.
[27] S. J. Blanksby, G. B. Ellison, *Acc. Chem. Res.* **2003**, *36*, 255.
[28] S. Bailey, D. Visontai, C. J. Lambert, M. R. Bryce, H. Frampton, D. Chappell, *J. Chem. Phys.* **2014**, *140*, 054708.

[29] Y. Zhu, Y. Hao, E. A. Adogla, J. Yan, D. Li, K. Xu, Q. Wang, J. Hone, Q. Lin, *Nanoscale* **2016**, Ahead of Print; J. Wang, H. Zhu, Y. Xu, W. Yang, A. Liu, F. Shan, M. Cao, J. Liu, *Sens. Actuators, B* **2015**, *220*, 1186.
[30] H. Zhang, Y. Wang, D. Zhao, D. Zeng, J. Xia, A. Aldalbahi, C. Wang, L. San, C. Fan, X. Zuo, X. Mi, *ACS Appl. Mater. Interfaces* **2015**, *7*, 16152.
[31] A. Perry, S. J. Green, D. W. Horsell, S. M. Hornett, M. E. Wood, *Tetrahedron* **2015**, *71*, 6776.
[32] S. Li, X. Zhong, H. Yang, Y. Hu, F. Zhang, Z. Niu, W. Hu, Z. Dong, J. Jin, R. Li, J. Ma, *Carbon* **2011**, *49*, 4239.
[33] R. Mazzaro, M. Locritani, J. K. Molloy, M. Montalti, Y. Yu, B. A. Korgel, G. Bergamini, V. Morandi, P. Ceroni, *Chem. Mater.* **2015**, *27*, 4390; C. Ingrosso, G. V. Bianco, M. Corricelli, R. Comparelli, D. Altamura, A. Agostiano, M. Striccoli, M. Losurdo, M. L. Curri, G. Bruno, *ACS Appl. Mater. Interfaces* **2015**, *7*, 4151.
[34] L. Cambi, L. Szegö, *Berichte der deutschen chemischen Gesellschaft (A and B Series)* **1931**, *64*, 2591.
[35] G. A. Melson, D. H. Busch, *J. Am. Chem. Soc.* **1964**, *86*, 4830.
[36] R. C. Stoufer, D. H. Busch, W. B. Hadley, *J. Am. Chem. Soc.* **1961**, *83*, 3732; J. S. Judge, W. A. Baker, Jr., *Inorg. Chim. Acta* **1967**, *1*, 68; M. Bacci, F. Mani, S. Midollini, *Gazz. Chim. Ital.* **1972**, *102*, 1019.
[37] G. A. Renovitch, W. A. Baker, Jr., *J. Am. Chem. Soc.* **1967**, *89*, 6377; P. Spacu, M. Teodorescu, G. Filotti, P. Telnic, *Z. Anorg. Allg. Chem.* **1972**, *392*, 88; P. Spacu, M. Teodorescu, D. Ciomartan, *Monatsh. Chem.* **1972**, *103*, 1.
[38] E. V. Dose, K. M. M. Murphy, L. J. Wilson, *Inorg. Chem.* **1976**, *15*, 2622; V. I. Shipilov, V. V. Zelentsov, A. V. Ablov, N. V. Gerbeleu, C. V. Dyatlova, *Teor. Eksp. Khim.* **1975**, *11*, 781; M. F. Tweedle, L. J. Wilson, *J. Am. Chem. Soc.* **1976**, *98*, 4824.
[39] J. H. Ammeter, R. Bucher, N. Oswald, *J. Am. Chem. Soc.* **1974**, *96*, 7833; J. H. Ammeter, N. Oswald, R. Bucher, D. Von Arx, *Chimia* **1975**, *29*, 525.
[40] O. Kahn, C. J. Martinez, *Science* **1998**, *279*, 44.
[41] M. A. Halcrow, *Chem. Lett.* **2014**, *43*, 1178.
[42] S. Decurtins, P. Gütlich, C. P. Köhler, H. Spiering, A. Hauser, *Chem. Phys. Lett.* **1984**, *105*, 1; A. Hauser, *Chem. Phys. Lett.* **1986**, *124*, 543.
[43] H. J. Shepherd, S. Bonnet, P. Guionneau, S. Bedoui, G. Garbarino, W. Nicolazzi, A. Bousseksou, G. Molnar, *Phys. Rev. B: Condens. Matter Mater. Phys.* **2011**, *84*, 144107/1.
[44] A. Bousseksou, N. Negre, M. Goiran, L. Salmon, J.-P. Tuchagues, M.-L. Boillot, K. Boukheddaden, F. Varret, *The European Physical Journal B - Condensed Matter and Complex Systems* **2000**, *13*, 451.
[45] C. Lefter, R. Tan, J. Dugay, S. Tricard, G. Molnár, L. Salmon, J. Carrey, W. Nicolazzi, A. Rotaru, A. Bousseksou, *Chem. Phys. Lett.* **2016**, *644*, 138.
[46] F. Prins, M. Monrabal-Capilla, E. A. Osorio, E. Coronado, H. S. J. van der Zant, *Adv. Mater.* **2011**, *23*, 1545.
[47] L. E. Orgel, *The Journal of Chemical Physics* **1955**, *23*, 1819.
[48] L. G. Vanquickenborne, L. Haspeslagh, *Inorg. Chem.* **1982**, *21*, 2448.
[49] O. Kahn, *VCH Publishers, Inc.(USA), 1993* **1993**, 393.
[50] P. Gütlich, A. B. Gaspar, Y. Garcia, *Beilstein J. Org. Chem.* **2013**, *9*, 342.
[51] S. Bonnet, M. A. Siegler, J. S. Costa, G. Molnar, A. Bousseksou, A. L. Spek, P. Gamez, J. Reedijk, *Chem. Commun. (Cambridge, U. K.)* **2008**, 5619.
[52] H. Spiering, K. Boukheddaden, J. Linares, F. Varret, *Phys. Rev. B* **2004**, *70*, 184106.
[53] K. Ridier, G. Molnár, L. Salmon, W. Nicolazzi, A. Bousseksou, *Solid State Sci.* **2017**, *74*, A1.
[54] M. A. Halcrow, *Chem. Soc. Rev.* **2011**, *40*, 4119.
[55] S. Zheng, N. R. M. Reintjens, M. A. Siegler, O. Roubeau, E. Bouwman, A. Rudavskyi, R. W. A. Havenith, S. Bonnet, *Chem. - Eur. J.* **2016**, *22*, 331.
[56] Z. Arcis-Castíllo, S. Zheng, M. A. Siegler, O. Roubeau, S. Bedoui, S. Bonnet, *Chem. Eur. J.* **2011**, *17*, 14826.

[57] S. Zheng, N. R. M. Reintjens, M. A. Siegler, O. Roubeau, E. Bouwman, A. Rudavskyi, R. W. A. Havenith, S. Bonnet, *Chem. Eur. J.* **2016**, *22*, 331.
[58] M. Mikolasek, G. Felix, W. Nicolazzi, G. Molnar, L. Salmon, A. Bousseksou, *New J. Chem.* **2014**, *38*, 1834.
[59] A. Muraoka, J. Linares, K. Boukheddaden, "Monte Carlo simulation of the Ising-like model on size and surface effects in the spin crossover nanoparticles", 2010; A. Muraoka, K. Boukheddaden, *Mater. Sci. Forum* **2014**, *793*, 77; A. Atitoaie, R. Tanasa, C. Enachescu, *J. Magn. Magn. Mater.* **2012**, *324*, 1596.
[60] G. Molnár, S. Rat, L. Salmon, W. Nicolazzi, A. Bousseksou, *Adv. Mater.* **2018**, *30*, 1703862.
[61] F. Volatron, L. Catala, E. Rivière, A. Gloter, O. Stéphan, T. Mallah, *Inorg. Chem.* **2008**, *47*, 6584.
[62] A. Grosjean, N. Daro, B. Kauffmann, A. Kaiba, J.-F. Letard, P. Guionneau, *Chem. Commun.* **2011**, *47*, 12382.
[63] A. Rotaru, F. Varret, A. Gindulescu, J. Linares, A. Stancu, J. F. Létard, T. Forestier, C. Etrillard, *Eur. Phys. J. B* **2011**, *84*, 439.
[64] T. Forestier, A. Kaiba, S. Pechev, D. Denux, P. Guionneau, C. Etrillard, N. Daro, E. Freysz, J.-F. Létard, *Chem. Eur. J.* **2009**, *15*, 6122.
[65] J. R. Galan-Mascaros, E. Coronado, A. Forment-Aliaga, M. Monrabal-Capilla, E. Pinilla-Cienfuegos, M. Ceolin, *Inorg. Chem.* **2010**, *49*, 5706; E. Coronado, J. R. Galán-Mascarós, M. Monrabal-Capilla, J. García-Martínez, P. Pardo-Ibáñez, *Adv. Mater.* **2007**, *19*, 1359.
[66] J. Linares, C.-M. Jureschi, A. Boulmaali, K. Boukheddaden, *Physica B Condens.* **2016**, *486*, 164.
[67] Y. Raza, F. Volatron, S. Moldovan, O. Ersen, V. Huc, C. Martini, F. Brisset, A. Gloter, O. Stéphan, A. Bousseksou, L. Catala, T. Mallah, *Chem. Commun.* **2011**, *47*, 11501.
[68] S. Cobo, G. Molnár, J. A. Real, A. Bousseksou, *Angew. Chem., Int. Ed.* **2006**, *45*, 5786.
[69] S. Shi, G. Schmerber, J. Arabski, J. B. Beaufrand, D. J. Kim, S. Boukari, M. Bowen, N. T. Kemp, N. Viart, G. Rogez, E. Beaurepaire, H. Aubriet, J. Petersen, C. Becker, D. Ruch, *Appl. Phys. Lett.* **2009**, *95*, 043303.
[70] M. Cavallini, *Phys. Chem. Chem. Phys.* **2012**, *14*, 11867.
[71] T. G. Gopakumar, F. Matino, H. Naggert, A. Bannwarth, F. Tuczek, R. Berndt, *Angew. Chem., Int. Ed.* **2012**, *51*, 6262.
[72] A. Bousseksou, G. Molnar, L. Salmon, W. Nicolazzi, *Chem. Soc. Rev.* **2011**, *40*, 3313; G. J. Dolan, *Appl. Phys. Lett.* **1977**, *31*, 337.
[73] G. Molnár, S. Cobo, J. A. Real, F. Carcenac, E. Daran, C. Vieu, A. Bousseksou, *Adv. Mater.* **2007**, *19*, 2163.
[74] J. Dugay, M. Giménez-Marqués, T. Kozlova, H. W. Zandbergen, E. Coronado, H. S. J. van der Zant, *Adv. Mater.* **2015**, *27*, 1288.
[75] G. Felix, K. Abdul-Kader, T. Mahfoud, I. y. A. Gural'skiy, W. Nicolazzi, L. Salmon, G. Molnar, A. Bousseksou, *J. Am. Chem. Soc.* **2011**, *133*, 15342.
[76] I. y. A. Gural'skiy, C. M. Quintero, K. Abdul-Kader, M. Lopes, C. Bartual-Murgui, L. Salmon, P. Zhao, G. Molnar, D. Astruc, A. Bousseksoua, *J. Nanophotonics* **2012**, *6*, 063517.
[77] C. Bartual-Murgui, A. Cerf, C. Thibault, C. Vieu, L. Salmon, G. Molnar, A. Bousseksou, *Microelectron. Eng.* **2013**, *111*, 365.
[78] A. Grohmann, M. Haryono, K. Student, P. Mueller, M. Stocker, *Eur. J. Inorg. Chem.* **2013**, *2013*, 662.
[79] A. C. Aragones, D. Aravena, J. I. Cerda, Z. Acis-Castillo, H. Li, J. A. Real, F. Sanz, J. Hihath, E. Ruiz, I. Diez-Perez, *Nano Lett.* **2016**, *16*, 218; G. D. Harzmann, R. Frisenda, H. S. J. van der Zant, M. Mayor, *Angew. Chem., Int. Ed.* **2015**, *54*, 13425.
[80] K. Senthil Kumar, M. Ruben, *Coord. Chem. Rev.* **2017**, *346*, 176.
[81] J. J. Rack, J. R. Winkler, H. B. Gray, *J. Am. Chem. Soc.* **2001**, *123*, 2432; A. A. Rachford, J. L. Petersen, J. J. Rack, *Inorg. Chem.* **2005**, *44*, 8065; J. J. Rack, A. A. Rachford, A. M. Shelker, *Inorg. Chem.* **2003**, *42*, 7357.
[82] A. Chaudhary, A. Mohammad, S. M. Mobin, *Cryst. Growth Des.* **2017**, *17*, 2893.

[83] M. D. Manrique-Juárez, S. Rat, L. Salmon, G. Molnár, C. M. Quintero, L. Nicu, H. J. Shepherd, A. Bousseksou, *Coord. Chem. Rev.* **2016**, *308*, 395.
[84] S. L. Hopkins, S. Bonnet, *Ligand Photosubstitution Reactions with Ruthenium Compounds*, in *Ruthenium Complexes*, Wiley-VCH Verlag GmbH & Co. KGaA, **2017**, 89; J. K. White, R. H. Schmehl, C. Turro, *Inorg. Chim. Acta* **2017**, *454*, 7; H. B. Ross, M. Boldaji, D. P. Rillema, C. B. Blanton, R. P. White, *Inorg. Chem.* **1989**, *28*, 1013.
[85] R. E. Goldbach, I. Rodriguez-Garcia, J. H. van Lenthe, M. A. Siegler, S. Bonnet, *Chem. Eur. J.* **2011**, *17*, 9924; D. V. Pinnick, B. Durham, *Inorg. Chem.* **1984**, *23*, 1440.
[86] R. N. Garner, L. E. Joyce, C. Turro, *Inorg. Chem.* **2011**, *50*, 4384.
[87] L. N. Lameijer, D. Ernst, S. L. Hopkins, M. S. Meijer, S. H. C. Askes, S. E. Le Dévédec, S. Bonnet, *Angew. Chem., Int. Ed.* **2017**, *56*, 11549; S. Bonnet, *Dalton Trans.* **2018**, *47*, 10330; B. S. Howerton, D. K. Heidary, E. C. Glazer, *J. Am. Chem. Soc.* **2012**, *134*, 8324; A. Li, C. Turro, J. J. Kodanko, *Acc. Chem. Res.* **2018**, *51*, 1415; A. Li, R. Yadav, J. K. White, M. K. Herroon, B. P. Callahan, I. Podgorski, C. Turro, E. E. Scott, J. J. Kodanko, *Chem. Commun.* **2017**, *53*, 3673; T. Respondek, R. N. Garner, M. K. Herroon, I. Podgorski, C. Turro, J. J. Kodanko, *J. Am. Chem. Soc.* **2011**, *133*, 17164; R. N. Garner, J. C. Gallucci, K. R. Dunbar, C. Turro, *Inorg. Chem.* **2011**, *50*, 9213; A. Li, C. Turro, J. J. Kodanko, *Chem. Commun.* **2018**, *54*, 1280.
[88] M. R. Gill, J. A. Thomas, *Chem. Soc. Rev.* **2012**, *41*, 3179.
[89] R. E. Morris, R. E. Aird, P. D. Murdoch, H. M. Chen, J. Cummings, N. D. Hughes, S. Parsons, A. Parkin, G. Boyd, D. I. Jodrell, P. J. Sadler, *J. Med. Chem.* **2001**, *44*, 3616; H.-K. Liu, S. J. Berners-Price, F. Wang, J. A. Parkinson, J. Xu, J. Bella, P. J. Sadler, *Angew. Chem., Int. Ed.* **2006**, *45*, 8153; Z. Adhireksan, G. E. Davey, P. Campomanes, M. Groessl, C. M. Clavel, H. Yu, A. A. Nazarov, C. H. F. Yeo, W. H. Ang, P. Dröge, U. Rothlisberger, P. J. Dyson, C. A. Davey, *Nat. Commun.* **2014**, *5*, 3462.
[90] H. Chan, J. B. Ghrayche, J. Wei, A. K. Renfrew, *Eur. J. Inorg. Chem.* **2017**, *2017*, 1679.
[91] M. G. Walker, V. Ramu, A. J. H. M. Meijer, A. Das, J. A. Thomas, *Dalton Trans.* **2017**, *46*, 6079; A. E. Friedman, J. C. Chambron, J. P. Sauvage, N. J. Turro, J. K. Barton, *J. Am. Chem. Soc.* **1990**, *112*, 4960; C. Hiort, P. Lincoln, B. Norden, *J. Am. Chem. Soc.* **1993**, *115*, 3448; A. N. Boynton, L. Marcélis, J. K. Barton, *J. Am. Chem. Soc.* **2016**, *138*, 5020.
[92] V. Rajendiran, M. Palaniandavar, V. S. Periasamy, M. A. Akbarsha, *J. Inorg. Biochem.* **2010**, *104*, 217.
[93] V. Gonzalez, T. Wilson, I. Kurihara, A. Imai, J. A. Thomas, J. Otsuki, *Chem. Commun.* **2008**, 1868.
[94] E. Wachter, D. Moyá, S. Parkin, E. C. Glazer, *Chem. Eur. J.* **2016**, *22*, 550.